

Investigation of signature inversion in ^{126}I through lifetime measurements

Himanshu Kumar Singh, Pragya Das^{✉,*} and Bhushan A. Kanagalekar[†]

Department of Physics, Indian Institute of Technology Bombay, Powai, Mumbai 400076, India

S. Muralithar and R. P. Singh

Inter-University Accelerator Centre, Aruna Asaf Ali Marg, New Delhi 110067, India



(Received 14 February 2019; revised manuscript received 25 September 2019; published 9 December 2019)

The reduced transition probabilities $B(E2)$ and $B(M1)$ of the negative-parity yrast states of ^{126}I were studied by measuring the lifetimes in picoseconds using the Doppler-shift attenuation method. We investigated the phenomena of signature splitting and inversion using the two quasiparticle-plus triaxial rotor model (PRM). The experimental result—a sharp decrease in the $B(E2)$ values at the signature inversion—indicated a shape change with a possible shift in the axis of rotation. We interpreted this observation as a change in the triaxiality parameter, with values $\gamma = -10^\circ$ (Lund convention) below the inversion and $\gamma = 25^\circ$ above it and a constant value of axial deformation of $\beta \approx 0.15$. We also assigned the valence particle configuration—neutron in the $h_{11/2}$ orbital and proton predominantly in the $d_{5/2}$ orbital mixed with the $g_{7/2}$ orbital—from the PRM calculation. Furthermore, the calculation reproduced the overall observed behavior of the signature splitting and inversion reasonably well. The observed backbending at the rotational frequency of 0.47 MeV was due to neutron alignment consistent with the second band crossing from the quasiparticle Routhian diagram.

DOI: [10.1103/PhysRevC.100.064306](https://doi.org/10.1103/PhysRevC.100.064306)

I. INTRODUCTION

In the mass region of ≈ 130 , the doubly-odd nuclei exhibit many nuclear phenomena, such as signature splitting and inversion, backbending, decoupled band, chirality, and many more [1–5]. Among all these, much studied are the signature splitting and inversion in rotational spectra of nuclei [6]. Due to collective rotation $R_z(\pi)$ around the principal axis, often the band with the angular momentum difference $\Delta I = 1$ is resolved into two signature partner bands of even- and odd-spin states with $\Delta I = 2$. The two bands are energetically favored and unfavored due to the interaction of the Coriolis force with the rotating body. Favored energy states have less energy than unfavored ones, leading to “normal” signature splitting. However, in some cases, the phenomenon is reversed, known as “anomalous” signature splitting. Anomalous (normal) signature splitting gets flipped to normal (anomalous) splitting at a critical spin (I_c)—a phenomenon known as signature inversion. It is of interest to observe which way the flipping occurs and to understand the underlying physics. Earlier Bengtsson *et al.* [7] suggested a theoretical treatment using the cranked shell model (CSM) calculations to explain signature inversion as a result of the change in deformation of triaxial nuclei. Hamamoto [8] proposed a different argument using quasiparticle-plus rotor model (PRM) calculations; it elucidates that the triaxial deformation is not

a crucial factor for the signature splitting and inversion. With the same model, Ikeda *et al.* [9,10] suggested that the cause of signature inversion is due to a change in the axis of rotation from intermediate to short. Further work using an axially deformed core suggested the reason for signature inversion as a mechanism of Coriolis mixing of multiple bands [11,12]. In essence, no unique mechanism exists conclusively; therefore the phenomenon of signature inversion still stands as an open problem.

The context of the present work is to investigate signature inversion in the negative-parity yrast states of ^{126}I through lifetime measurement. The spectroscopic study of ^{126}I suggests 2^+ (J^π) [13] as its ground state. With the possibility of valence particles (protons and neutrons) lying in various Nilsson orbits in a triaxial core nucleus, characterized by the deformation parameters (β , γ) [14], the nucleus ^{126}I is a good candidate for shape coexistence. Chiral bands—with roughly matching excitation energies—possibly exist as supported by some theoretical calculations [14,15]. Earlier works [14,16] reported the signature splitting and inversion at $I_c = 13\hbar$ in the yrast band. The band is built by the valence neutron in the intruder orbit $h_{11/2}$; whereas a mixed configuration exists for the valence proton involving the orbitals $d_{5/2}$ and $g_{7/2}$. Indeed, we have argued $d_{5/2}$ as the predominant valence proton configuration in our earlier work [14] solely based on the theoretical analysis. Using yet another theoretical model, Zheng *et al.* [16] found $g_{7/2}$ to be the predominant proton configuration. In the present work, we have focused on getting a definitive answer to the nuclear shape parameters and their effect on the configuration mixing of the valence proton through the measurement of lifetimes.

*Pragya@phy.iitb.ac.in

[†]Present address: Department of Physics, Rani Channamma University, Belgavi 590006, India.

We used the Doppler-shift attenuation method (DSAM) to measure lifetimes of ^{126}I . The Doppler-shift method is widely used to gauge lifetimes in the picoseconds range [17,18]. We analyzed the data using two different gating methods, GTB (gating on transition below) and GTA (gating on transition above), as described in the literature [19–21]. The GTB method yielded good statistics of data, while the GTA method was free of side-feeding parameters. Further, the lifetime results were verified using two detector angles—one forward and another backward in direction. From the measured transition probabilities, we inferred triaxially deformed nuclear shapes. Using the experimentally derived shape parameters, we performed theoretical calculations based on the two quasiparticle-plus triaxial rotor model. It seems signature inversion happened due to nuclear shape change with a shift in the rotational axis. We achieved the correct phase of the signature splitting, but much less the extent of theoretical splitting than the experimental results below inversion. Further about the calculation results, $d_{5/2}$ was found as the dominant valence proton configuration mixed with $g_{7/2}$, coupled with an $h_{11/2}$ valence neutron. We, therefore, remained consistent with our earlier result [14] of the anomalous splitting becoming normal above the inversion, satisfying the cranking picture of the nuclear model.

II. EXPERIMENTAL DETAILS

The high-spin states of ^{126}I were populated by the fusion-evaporation reaction $^{124}\text{Sn}(^7\text{Li}, 5n)^{126}\text{I}$ at the incident beam energy of 50 MeV from the Pelletron accelerator at the Inter-University Accelerator Center, New Delhi, India. An enriched (99.4%) ^{124}Sn foil of thickness 2.7 mg/cm² acted as the self-supporting target without any other backing material. Because the reaction proceeded at the high beam energy compared with the Coulomb barrier (~ 28 MeV), the recoiling nuclei received sufficient velocity to move in the target. The average recoil velocity was estimated to be 0.67% of the speed of light. Fifteen Compton-suppressed high-purity germanium Clover detectors—at angles of 32°, 57°, 90°, 123°, and 148° with respect to the beam direction—installed in the Indian National Gamma Array [22], constituted the experimental setup to detect the emitted γ rays. The list mode data were collected by the CAMAC based in-house software CANDLE [23] and processed in LAMPS [24] software for creating matrices. More experimental details were presented in our earlier work [14]. We utilized the data corresponding to three rings, 32° (three detectors), 90° (four detectors), and 148° (four detectors), to create asymmetric matrices and sorted them in the angle of interest detector vs all detectors. We thus analyzed the Doppler lineshapes using three asymmetric matrices: 32° vs all to observe forward Doppler shift, 148° vs all to observe backward shift, and 90° vs all to examine the nearby γ peaks as contaminants.

III. DATA ANALYSIS

A. Thick target and Doppler-broadening correction

The choice of target thickness is vital for the DSAM. Researchers have often used thin targets with a backing (stopper)

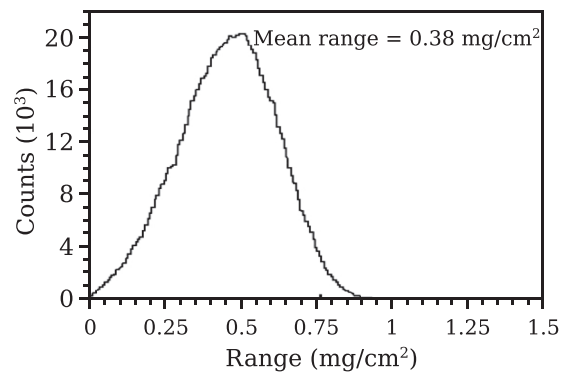


FIG. 1. Recoil range distribution of ^{126}I in ^{124}Sn calculated using the SRIM-2008 [26] software package.

that stops all the recoiling nuclei. A thin target with a stopper (high- Z material), however, has several limitations. Unless the target is infinitesimally thin, the use of two different materials increases the complexity of the stopping power information; therefore the energy loss in the target is often ignored. Moreover, the possibility of the target completely stopping the recoils cannot be ruled out. Furthermore, it is difficult to make a thin and uniform target and at the same time avoid any gap between the target and the stopper. Also, if the beam energy is sufficiently high (above the Coulomb barrier of a projectile and the backing material), many unwanted reaction channels open up. As a consequence, the overlapping γ peaks appear as contaminants to the peak of interest, making the DSAM lineshape analysis a cumbersome task.

On the other hand, a self-supporting thick target—much less utilized usually—can also act as the stopper with minimal relative nonuniformity, also taking care of all the other shortcomings mentioned above. However, a thick target does not ensure the stopping of all the recoiling nuclei in some cases. In other words, a thick target [25] can be used when the stopping time is of the order of lifetimes—applicable for our experiment with the ^{124}Sn target foil (2.7 mg/cm²). The only limitation was to incorporate the continuous production and stopping of the recoils in the target. By assuming that the reaction occurred at the surface of the target, the average recoil range in the target was found to be 0.38 mg/cm², as shown in Fig. 1, using the SRIM-2008 software package [26]. We estimated roughly 15% of the recoils flying off in vacuum by considering six to seven layers of the target, each layer of thickness roughly the range of recoils. This percentage value got reduced substantially because the population of the $5n$ channel decreased sharply with beam energy, roughly half as the beam energy decreased to 46 MeV, implying a substantial decrease in production in the subsequent layers of target. In effect, a statistical uncertainty of approximately 5% could take care of both the continuous production and the stopping of the recoils in the target assuming the normal population distribution.

Another aspect of a thick target experiment is the Doppler broadening in γ -ray energies. The broadening is due to the detector resolution, straggling in the velocity distributions of recoils (kinematic Doppler broadening), and the finite opening

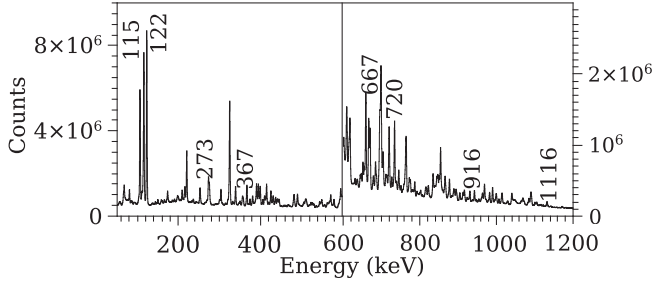


FIG. 2. Total projected spectrum with marked peaks (energy in keV) used for finding the Doppler broadening.

angle of the detector; writing it mathematically, we get

$$\left(\frac{\Delta E_0}{E_0}\right)^2 = \left(\frac{\beta\gamma^2(\beta - \cos\theta_{\text{lab}})}{1 - \beta\cos\theta_{\text{lab}}}\right)^2 \left(\frac{\Delta\beta}{\beta}\right)^2 + \left(\frac{\Delta E}{E}\right)^2 + \left(\frac{\beta\sin\theta_{\text{lab}}}{1 - \beta\cos\theta_{\text{lab}}}\right)^2 (\Delta\theta_{\text{lab}})^2, \quad (1)$$

where ΔE_0 is the broadening in the γ -ray energy (E_0), $\Delta E/E$ is the fractional spread due to the detector resolution, $\Delta\theta_{\text{lab}}$ is the opening angle of the detector, $\gamma = \frac{1}{\sqrt{1-\beta^2}}$ is the Lorentz factor, and $\beta = v/c$. Instead of utilizing the complex equation (1) [27], we estimated the percentage broadening directly from the experimental data using Eq. (2), given as

$$\text{DB}(\%) = \frac{\text{FWHM}_{\text{on}} - \text{FWHM}_{\text{off}}}{\text{FWHM}_{\text{off}}} \times 100. \quad (2)$$

The values of FWHM_{on} (full width at half maximum) in Eq. (2) were obtained by choosing well-separated γ peaks belonging to ^{126}I in the total projected spectrum (Fig. 2) from the symmetric matrix of the online data. Corresponding to the same γ -energy values, we calculated FWHM_{off} (Table I) by interpolating the FWHM vs energy curve of standard radioactive source ^{152}Eu (off-line) data. The error in the quoted values of FWHM was $\leq 0.8\%$. The Doppler-broadened FWHM depends upon the γ -ray energy. However, the percentage Doppler broadening (DB in %) turned out to be more or less constant, $\approx 9.45\%$ (average value), as shown in Fig. 3 and Table I. The average DB was calculated from the area under the curve using the trapezoidal rule.

TABLE I. Doppler broadening (DB in %) in γ -ray energies emitted from the recoiling ^{126}I nuclei; see details in the text.

E_γ (keV)	FWHM_{on} (keV)	FWHM_{off} (keV)	DB (%)
115	1.86	1.70	9.26 \pm 1.24
122	1.87	1.71	8.72 \pm 1.23
273	2.12	1.93	9.83 \pm 1.24
367	2.20	2.02	8.54 \pm 1.24
667	2.49	2.29	9.26 \pm 1.23
720	2.58	2.33	10.99 \pm 1.26
916	2.66	2.45	7.99 \pm 1.22
1116	2.90	2.58	12.50 \pm 1.27

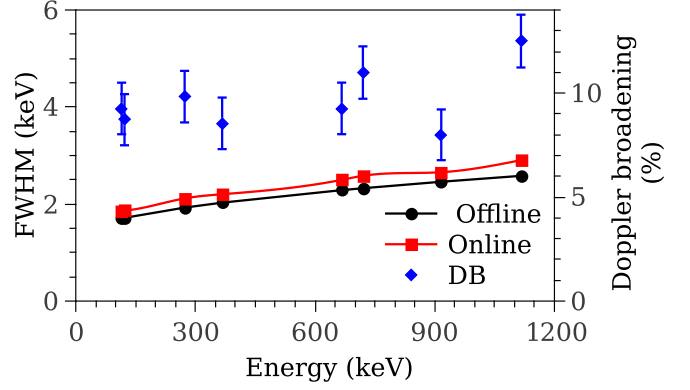


FIG. 3. The energy FWHM and Doppler broadening (DB in %) plotted as a function of γ -ray energy. The data were from the radioactive source ^{152}Eu (off-line) and the total projected spectrum (on-line data in Fig. 2).

B. Branching ratios and side-feeding intensities

Figure 4 presents the partial decay scheme of ^{126}I . The intensities, spins, and parities were determined earlier from the symmetric and asymmetric matrices, cubes, as described in earlier works [14–16]. We doubly checked the intensities of relevant γ transitions by gating on an intense low-lying transition using the symmetric matrix. The side-feeding intensities were calculated by taking the difference between the depopulating intensities and the populating intensities using the following formula:

$$I_\gamma(\text{SF}) = I_\gamma(I \rightarrow I-2) + I_\gamma(I \rightarrow I-1) - I_\gamma(I+2 \rightarrow I) - I_\gamma(I+1 \rightarrow I). \quad (3)$$

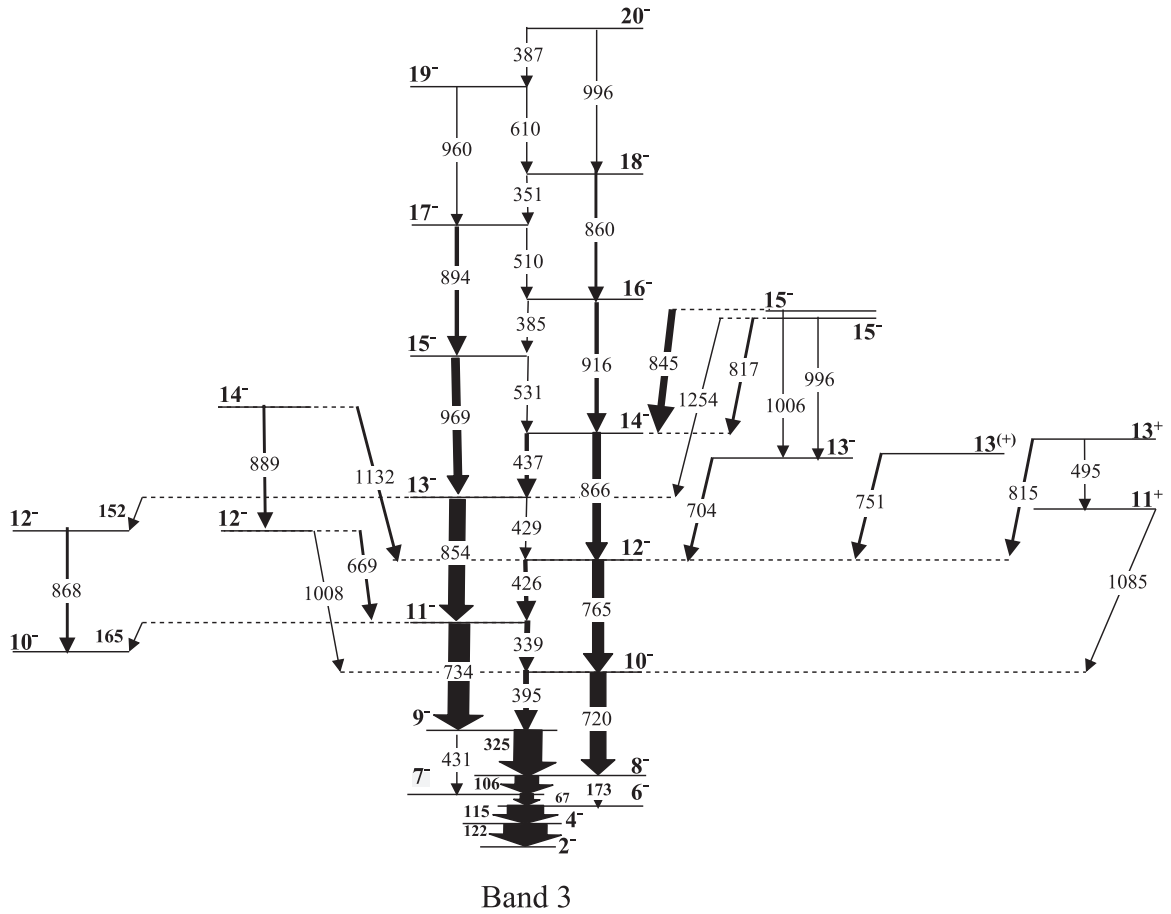
The side-feeding intensities increased smoothly with increasing spin, except at $12\hbar$, for which the value was found to be unphysical (negative value). We, therefore, interpolated the value at $12\hbar$ (marked as * in Table II) from the side-feeding curve as a function of spin. The branching ratios were calculated using the following equation,

$$f_\gamma(E2) = \frac{I_\gamma(I \rightarrow I-2)}{I_\gamma(I \rightarrow I-2) + I_\gamma(I \rightarrow I-1)}, \quad (4)$$

and are listed in Table II. It is noteworthy that the $M1$ transitions decaying from odd spins to even spins were found

TABLE II. Branching ratio and side-feeding intensity of the γ rays at various spins of ^{126}I . The value marked with * was obtained by interpolation.

$I^\pi(\hbar)$	E_γ (keV)	Branching ratio	Side-feeding (%)
10 ⁻	720	0.58	20.80
11 ⁻	734	0.69	24.82
12 ⁻	765	0.53	27.31*
13 ⁻	854	0.98	31.83
14 ⁻	866	0.57	34.79
15 ⁻	969	0.95	37.10
16 ⁻	916	0.65	39.42
17 ⁻	894	0.87	41.23


 FIG. 4. Yrast band and interband linking transitions belonging to ^{126}I .

to be weak as compared to the decays from even to odd; this could be one reason we observed a considerable change in the side-feeding intensities and branching ratios as a function of spin.

C. Side-feeding lifetimes

Another important parameter, besides branching ratios, is the side-feeding lifetimes (τ_{sf}). To obtain an initial guess of τ_{sf} , we used the computer program COMPA [28] and utilized an empirical relation [Eq. (5)]. The relation depends on the entry state energy [$E_{\text{entry}}(I_{\text{lev}})$] and the level energy (E_{lev}) for each spin (I_{lev}) and on the maximum angular momentum attained ($I_{\text{max}} \cong 34\hbar$) in the reaction:

$$\tau_{\text{sf}}(E_{\text{lev}}, I_{\text{lev}}) \approx 0.007(E_{\text{entry}}(I_{\text{lev}}) - E_{\text{lev}}) + 0.007(I_{\text{max}} - I_{\text{lev}}). \quad (5)$$

Figure 5 depicts the contour plot using COMPA [28] for the reaction $^{124}\text{Sn}(^7\text{Li}, 5n)^{126}\text{I}$ at $E_{\text{beam}} = 50$ MeV. The plot also indicates curves for the entry levels (dashed black curve) and energy levels (solid blue curve) corresponding to the yrast negative-parity states of ^{126}I . Table III lists the estimated side-feeding lifetimes.

D. Doppler-shift attenuation method

The Doppler shift in γ rays emitted from recoiling nuclei, as observed in the laboratory frame within the first-order approximation for $\beta \ll 1$, can be expressed as [17]

$$E_{\gamma} = E_{\gamma}^0(1 + \beta \cos \theta_{\text{lab}}), \quad (6)$$

where E_{γ} is the shifted γ -ray energy, E_{γ}^0 is its actual energy, $\beta = v/c$ is the recoil velocity, and θ_{lab} is the angle between

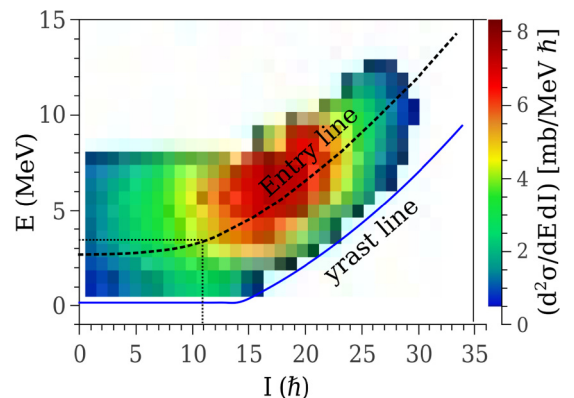


FIG. 5. Contour plot of excitation energy vs angular momentum obtained using the computer program COMPA [28].

TABLE III. Side-feeding lifetimes at various levels of the yrast band in ^{126}I .

I^π (\hbar)	Energy (keV)	τ_{sf} (ps)
10^-	720	0.18
11^-	734	0.17
12^-	765	0.16
13^-	854	0.15
14^-	866	0.14
15^-	969	0.13
16^-	916	0.12
17^-	894	0.11

the detector and the beam axis. The continuous deceleration of recoil nuclei in the stopping medium leads to a statistically skewed Gaussian profile in the low (high)-energy side of the actual γ -ray peak depending on the obtuse (acute) value of θ_{lab} . From these skewed Gaussian profiles—called the lineshapes—the lifetime values are determined using the DSAM.

In the DSAM, the Monte Carlo technique is utilized to generate lineshapes. We utilized the LINESHAPE software package of Wells and Johnson [29], built on two computer programs—DECHIST and HISTAVER. The program DECHIST simulates the time-dependent velocity profile in the target/backing medium corresponding to the given time step for all the simulated recoils. The “Northcliff and Schilling data table” [30] gives the stopping power information calculated from the Lindhard *et al.* [31–33] parametrization. The HISTAVER program uses this time-dependent velocity profile convoluted with the detector angle. Apart from the detector angle, the program needs the detector size and its distance from the target to estimate the solid angle. The efficiency of the detector was also required. Finally, the theoretically generated profiles were fitted to the experimental profiles using the LINESHAPE program. The program uses three χ^2 -minimization routines—SEEK, SIMPLEX, and MIGRAD—to evaluate lifetimes and their respective quadrupole moments. In our experimental data, eight transitions in the negative-parity yrast band, with energy values (in keV) of 720, 734, 765, 854, 866, 969, 916, and 894, exhibited lineshapes. We used several gates to generate the Doppler-shifted profiles from the two asymmetric matrices corresponding to the 32° and 148° detectors. The 90° detectors were also used for identifying the contaminants. Two different gating techniques, GTA and GTB, were used. At first, we carried out the analysis by gating on below transition (GTB) of interest. We tried to obtain the consistent results using two different models of side-feeding for the GTB analysis. The first model was a rotational model of the five-level cascade of constant dynamic moment of inertia and the second was the two-level model. We considered the same average dynamic moment of inertia—found to be $43 \text{ MeV}^{-1} \hbar^2$ —of the side-feeding and main bands, calculated from the following formula [34]:

$$\xi_d(I) = \frac{4\hbar^2}{E(I+2, I) - E(I, I-2)}, \quad (7)$$

where the denominator represents the difference of two γ -ray energies decaying between the states of spin values given inside the brackets. For the two-level side-feeding model, we fixed one level lifetime to the value estimated from the empirical relation [Eq. (5)], while varying the lifetime of other level during the fit. Both the models provide a sound understanding of the side-feeding lifetimes. However, it is often desirable to avoid side-feeding contributions to minimize the error in results. Hence, we adopted the procedure of gating on the above transitions (GTA) also. The major limitation of GTA was the low intensities of γ peaks as compared to those observed in GTB. To improve γ intensities, we used summed gated spectra to get the Doppler-shifted profiles. The GTA was crucial for the uppermost levels because they usually have a relatively large contribution from the side-feedings. In both the analysis procedures (GTA and GTB), we fitted all the levels globally and simultaneously at two angles (32° and 148°), and at the same time we observed the contaminant peaks in the spectrum of 90° detectors. Contaminants were often handled by visualizing their similar intensity ratios to the main peak in all three angles, keeping in mind the angular correlation effects. Moreover, the Doppler broadening (Sec. III A) was taken into account while fitting. As mentioned earlier, we relied on the GTA analysis for the top level, which gave us the starting result. The whole cascade of eight levels was fitted, starting from top to bottom successively, by fixing parameters one by one and keeping the quadrupole moment and the lifetime free for the transition of interest and its side-feeder. Figure 6 presents a few examples of our final fitting of lineshapes using the Doppler-shift attenuation method.

The relation between the quadrupole moment and the lifetime is defined as

$$\tau = \frac{16\pi f_\gamma(E2 : I, I-2)}{61.2E_\gamma^5 Q_t^2 \text{CG}_{\text{IK}}^2}, \quad (8)$$

where E_γ is the transition energy, Q_t is the quadrupole moment, $f_\gamma(E2 : I, I-2)$ is the branching ratio, and CG_{IK} is the Clebsch Gordan coefficient defined as

$$\text{CG}_{\text{IK}}^2 = \frac{3}{8} \left(\frac{I(I-1)}{I^2 - 0.25} \frac{I^2 - K^2}{I^2} \frac{(I-1)^2 - K^2}{(I-1)^2} \right). \quad (9)$$

The value of K ($=6$) for the yrast band was determined using the “Gallagher-Moszkowski rule” [14,35]—the parallel coupling of angular momentum projections on the symmetric axis, i.e., $K_1 = 3/2$ and $K_2 = 9/2$ for the valence proton and the valence neutron, respectively.

Because the lifetime is inversely proportional to the square of quadrupole moment Q_t [Eq. (8)], the error in the quadrupole moment is two times the error in the lifetime; i.e., the uncertainty in one propagates in the other. We determined the error in the lifetime values by finding how the χ^2 got affected by changing the lifetime values using the MINOS subroutine of the LINESHAPE software package [29]. Finally, we arrived at the error value when the χ^2 increased by 1. This way, the error could be symmetric or asymmetric around the lifetime value depending upon the neck of the parabola. Table IV lists our results. In the quoted error, we did not

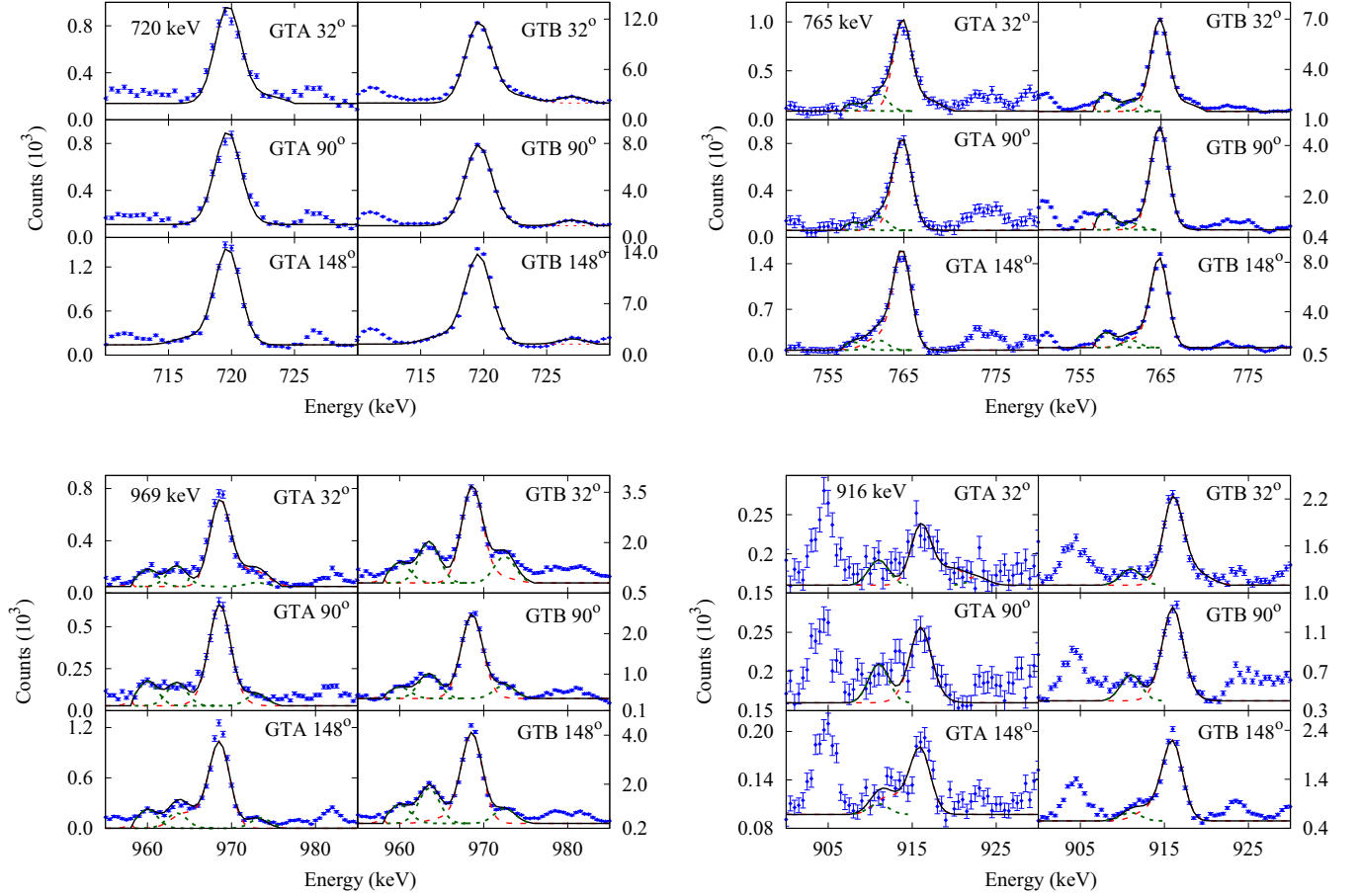


FIG. 6. Illustrative examples of lineshape fitting (in red) of the Doppler-shifted γ -peaks (in blue) obtained experimentally using gating above (GTA) and gating below (GTB) methods. The neighboring Gaussian-shaped contaminant peaks (green dashed curves) as well as total lineshapes profiles (black solid curves) are also shown.

include the error due to stopping power, which was approximately 15–20%. Another 5% error (mentioned in Sec. III A), due to continuous production and stopping of the recoils in the thick target, has also not been included.

We determined the reduced transition probabilities $B(E2)$ from the experimental lifetime values τ_{Avg} (Table IV) using Eq. (10). Further, $B(M1)$ values were calculated from the

mathematical expression [Eq. (11)] for the ratio of reduced transition probabilities:

$$B(E2) = \frac{0.0816 f_{\gamma}(E2)}{E_{\gamma}^5(E2)[1 + \alpha_t(E2)]\tau} [(e b)^2], \quad (10)$$

$$\frac{B(M1; I, I-1)}{B(E2; I, I-2)} = \frac{0.697 E_{\gamma}^5(I, I-2)}{\lambda E_{\gamma}^3(I, I-1)} \frac{1}{1 + \delta^2} \left[\frac{\mu_N^2}{e^2 b^2} \right], \quad (11)$$

TABLE IV. Summary of the lifetime results obtained using both gating above (GTA) and gating below (GTB) methods. The reduced transition probabilities $B(E2)$ and $B(M1)$ were obtained from the average of GTA and GTB results.

I^{π} (\hbar)	τ_{GTA} (ps)	τ_{GTB} (ps)	Q_{GTA} (e b)	Q_{GTB} (e b)	τ_{Avg} (ps)	Q_{Avg} (e b)	$B(E2)$ (e b) ²	$B(M1)$ (μ_N^2)
10 ⁻	1.48 ^{+0.11} _{-0.10}	1.01 ^{+0.17} _{-0.12}	4.87 ^{+0.17} _{-0.17}	5.93 ^{+0.07} _{-0.07}	1.24 ^{+0.20} _{-0.15}	5.40 ^{+0.18} _{-0.18}	0.20 ^{+0.05} _{-0.04}	0.10 ^{+0.025} _{-0.025}
11 ⁻	1.88 ^{+0.12} _{-0.13}	0.87 ^{+0.11} _{-0.13}	3.64 ^{+0.12} _{-0.12}	5.42 ^{+0.09} _{-0.10}	1.37 ^{+0.16} _{-0.18}	4.53 ^{+0.15} _{-0.16}	0.19 ^{+0.04} _{-0.04}	0.056 ^{+0.014} _{-0.014}
12 ⁻	2.76 ^{+0.08} _{-0.10}	2.56 ^{+0.08} _{-0.10}	2.50 ^{+0.05} _{-0.05}	2.59 ^{+0.03} _{-0.05}	2.66 ^{+0.11} _{-0.11}	2.54 ^{+0.06} _{-0.07}	0.06 ^{+0.01} _{-0.01}	0.037 ^{+0.006} _{-0.006}
13 ⁻	1.18 ^{+0.05} _{-0.06}	1.21 ^{+0.07} _{-0.09}	2.72 ^{+0.06} _{-0.06}	2.69 ^{+0.05} _{-0.09}	1.20 ^{+0.08} _{-0.11}	2.70 ^{+0.06} _{-0.08}	0.14 ^{+0.02} _{-0.02}	0.001 ^{+0.0001} _{-0.0001}
14 ⁻	2.24 ^{+0.08} _{-0.06}	2.07 ^{+0.18} _{-0.16}	1.83 ^{+0.03} _{-0.03}	1.90 ^{+0.03} _{-0.03}	2.16 ^{+0.20} _{-0.17}	1.87 ^{+0.04} _{-0.04}	0.03 ^{+0.01} _{-0.01}	0.016 ^{+0.052} _{-0.052}
15 ⁻	1.79 ^{+0.36} _{-0.26}	1.77 ^{+0.16} _{-0.11}	1.49 ^{+0.12} _{-0.13}	1.81 ^{+0.04} _{-0.04}	1.78 ^{+0.39} _{-0.28}	1.65 ^{+0.13} _{-0.14}	0.05 ^{+0.01} _{-0.01}	0.001 ^{+0.0002} _{-0.0002}
16 ⁻	1.62 ^{+0.15} _{-0.20}	1.65 ^{+0.14} _{-0.19}	1.75 ^{+0.12} _{-0.12}	1.74 ^{+0.04} _{-0.04}	1.64 ^{+0.20} _{-0.28}	1.74 ^{+0.13} _{-0.13}	0.05 ^{+0.01} _{-0.01}	0.020 ^{+0.004} _{-0.004}
17 ⁻	1.89 ^{+0.23} _{-0.16}	1.90 ^{+0.12} _{-0.09}	1.68 ^{+0.08} _{-0.09}	1.67 ^{+0.06} _{-0.06}	1.89 ^{+0.26} _{-0.18}	1.68 ^{+0.10} _{-0.11}	0.06 ^{+0.01} _{-0.01}	0.003 ^{+0.0005} _{-0.0005}

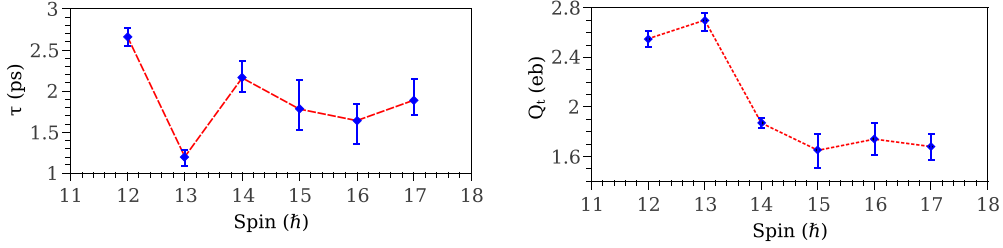


FIG. 7. Plots showing the lifetimes and quadrupole moments of the yrast states in ^{126}I .

where f_γ and α_t are the branching ratio and the total internal coefficient of the transition, λ is the intensity ratio of $E2$ and $M1$ transitions, and δ is the mixing ratio assumed to be 0. The values of α_t were considered to be 0 because of reasonably high energies of the γ transitions ($E_\gamma \geq 100$ keV). Table IV lists the calculated values of $B(E2)$ and $B(M1)$ along with the results on the lifetimes and quadrupole moments.

We plotted the quadrupole moment and lifetime values as a function of spin in Fig. 7. The trend in the values of the quadrupole moment is intriguing—almost a constant value ($2.6 e b$) below the signature inversion ($13\hbar$) and a sharply decreased value ($1.6 e b$), which remained constant again at high spins. The behavior is suggestive of a shape change at the inversion point, discussed theoretically in the next section.

IV. THEORETICAL DISCUSSION

A. Two quasiparticle-plus rotor model

1. Change in nuclear deformation at signature inversion

We theoretically studied the phenomenon of signature inversion in the light of our results on lifetimes. The two quasiparticle-plus rotor model [36,37], procured from Ranganarsson [38], was employed. We focused on understanding the change in the quadrupole moment after the signature inversion observed experimentally in Fig. 7. The deformation parameters were estimated using the following relation:

$$Q_t = \frac{3}{\sqrt{5}\pi} Z(r_0 A^{1/3})^2 \beta \frac{\cos(\gamma + 30^\circ)}{\cos(30^\circ)}. \quad (12)$$

In Eq. (12), we assumed a constant value of $\beta = 0.15$ [14,16] and $r_0 = 1.4$ fm, and we determined γ from the experimental values of the quadrupole moment (Q_t). The sign of γ was considered in the Lund convention [39] throughout our present study. Experimentally, we determined the average Q_t of roughly constant value in two regions—one below the signature inversion and another above (Fig. 7). It is noteworthy that we did not include the initial two spins ($10\hbar$ and $11\hbar$) for finding the average Q_t because of the mismatch in their values while using GTA and GTB analyses. Figure 8 exhibits a plot of Q_t vs γ using Eq. (12) and the experimentally measured average values are shown by thick hatched lines (in blue and green) incorporating errors. Further, two intersection points were found at $\gamma = -50^\circ$ (nearly oblate shape) and $\gamma = -10^\circ$ (nearly prolate shape) for spins below the signature inversion, whereas one intersection was found at $\gamma = 25^\circ$ (triaxial shape) for above the inversion. To perform the two quasiparticle-plus rotor model calculation, we needed

deformation parameters (β, γ) for the core and the single-particle energies for valence particles. In the first step, the single-particle energies and wave functions were calculated with the computer code [38] using a deformed harmonic potential or Nilsson potential. The program also utilizes the variable moment of inertia incorporating Harris parameters (ζ_0, ζ_1) [40,41]. These parameters were determined earlier by Kanagalekar *et al.* [14] for ^{126}I , and the values were $\zeta_0 = 22.4 \text{ MeV}^{-1} \hbar^2$ and $\zeta_1 = 36.6 \text{ MeV}^{-3} \hbar^4$.

In further calculation, we obtained the energy of the rotor of specified deformation parameters (β, γ) and coupled it with the single-particle energies to get the energy of the negative-parity yrast states of ^{126}I . A word of caution regarding the sign of γ is worth noting here. The particle rotor model code [38] uses the irrotational flow (IRF) kind of moment of inertia, defined as

$$\mathfrak{S}_k = \frac{4}{3} \mathfrak{S}_0 \sin^2 \left(\gamma + \frac{2}{3} \pi k \right), \quad (13)$$

where $k = 1, 2$, and 3 correspond to three principal axes of a triaxially deformed nucleus. For the minimum energy configuration, the expression leads to the rotation around the intermediate axis, in contrast to a rigid-body rotation around the shortest axis. We accordingly changed the sign of γ in the calculation. For instance, to utilize a negative value of γ in the Lund convention, we changed its sign to positive; whereas the positive value of γ in the Lund convention was treated as γ -reverse in the IRF model. In other words, we performed the calculation with the correct sign required for the IRF model in

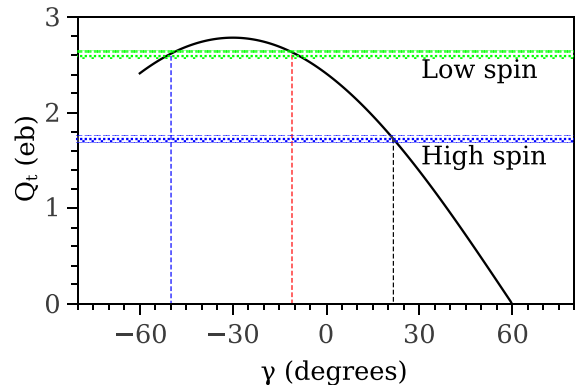


FIG. 8. Curve depicting the variation of the quadrupole moment with the triaxiality parameter γ (in the Lund convention) from Eq. (12). The hatched regions are the experimental average values below and above the signature inversion.

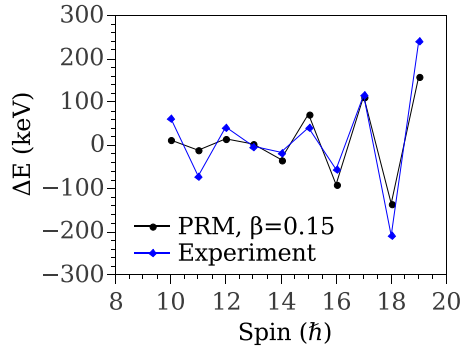


FIG. 9. Comparison of ΔE [defined in Eq. (14)] obtained experimentally and theoretically (PRM) showing the signature splitting and inversion.

our PRM calculation. However, to maintain the consistency and clarity, we have mentioned the sign of γ in the Lund convention always. In the following section, we discuss the results.

2. Comparison with experimental results

Experimentally, the signature inversion was found in the yrast negative-parity band of ^{126}I in earlier studies [14,16] with the mixed valence particle configurations $\pi d_{5/2} \otimes \nu h_{11/2}$ and $\pi g_{7/2} \otimes \nu h_{11/2}$. However, the dominant proton configuration was still a question of debate. Kanagalekar *et al.* [14] suggested $\pi d_{5/2} \otimes \nu h_{11/2}$ as the dominant configuration from the total Routhian surface (TRS) calculation leading to the normal signature inversion at high spins, whereas Zheng *et al.* [16] suggested $\pi g_{7/2} \otimes \nu h_{11/2}$ as the dominant configuration leading to the anomalous signature inversion. The former seemed to be the case in our present study. Signature splitting and inversion are recognized by plotting a function ΔE such as

$$\Delta E = [E(I) - E(I-1)] - \frac{1}{2}[E(I+1) - E(I) + E(I-1) - E(I-2)]. \quad (14)$$

In the two quasiparticle-plus rotor calculations, we used the estimated values of deformation ($\beta = 0.15$, $\gamma = -10^\circ$) at low spins and ($\beta = 0.15$, $\gamma = 25^\circ$) at spins above the inversion point. Simultaneously, we observed the contribution of various positive-parity orbits for the valence proton, while the valence neutron occupied the $h_{11/2}$ orbit. Figure 9 shows the experimental values compared with our theoretical results—for the mentioned two sets of deformation values for below and above the inversion—giving the correct phase of signature splitting. However, the extent of splitting was found to be small theoretically below the inversion. Besides, the PRM calculation predicted the dominant contribution of the $d_{5/2}$ orbital for the proton valence particle for both below and above the inversion point, presented in the pie chart (Fig. 10). Moreover, the calculation reproduced the sharp change in the experimental $B(E2)$ values at the inversion point reasonably well, better for $\beta = 0.13$ compared to $\beta = 0.15$, as seen in Fig. 11.

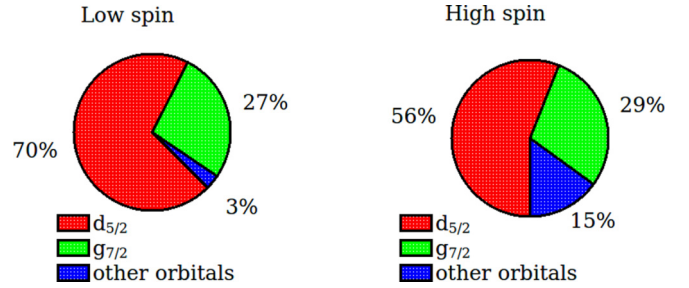


FIG. 10. Contribution of various positive-parity orbitals for the occupancy of the valence proton below (low spin) and above (high spin) the signature inversion in our PRM calculation.

It is worth mentioning that we made several attempts for the calculation. For instance, when we tried with the other possible value of triaxiality, $\gamma = -50^\circ$, below inversion obtained from the plot in Fig. 8, we were unable to reproduce the correct phase of the signature splitting for the predominant $\pi d_{5/2} \otimes \nu h_{11/2}$ configuration. It had to be predominantly the $\pi g_{7/2} \otimes \nu h_{11/2}$ configuration to get the correct phase. However, with the latter configuration we could not reconcile with the argument of observing normal signature splitting at high spins [14], consistent with the cranking picture. Moreover, the estimated value of g_{eff} by Kanagalekar *et al.* [14] was compatible with the former configuration predominantly. Intuitively also, such a large change in triaxiality, from $\gamma = -50^\circ$ (below) to $\gamma = 25^\circ$ (above) at the inversion, is unusual. We therefore discarded this deformation ($\beta = 0.15$, $\gamma = -50^\circ$). In another set of calculations, we tried an identical value of triaxiality below and above the inversion, ranging from $\gamma = 20^\circ$ to $\gamma = 30^\circ$, and the results could never reproduce the signature inversion no matter which positive-parity orbital we used for the proton occupancy.

B. Backbending and TRS calculation

We studied yet another phenomenon—backbending behavior of particle alignment with increasing rotational

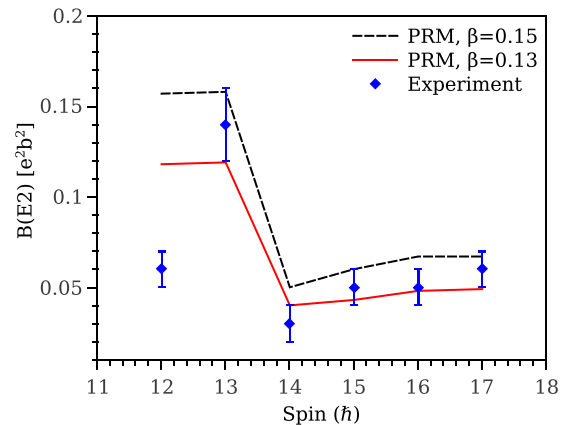


FIG. 11. Experimental and theoretical (PRM) values of the reduced transition probability $B(E2)$ showing a sharp change at the signature inversion.

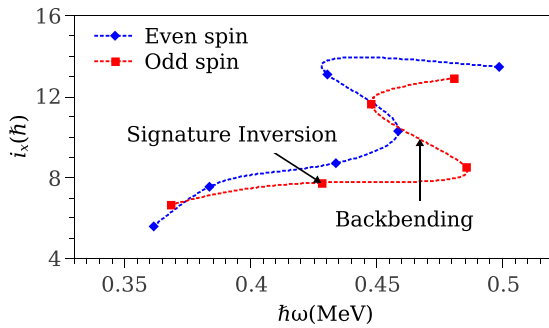


FIG. 12. Plot of rotational alignment (i_x) vs frequency ($\hbar\omega$) exhibiting the backbending at roughly the same frequency as signature inversion.

frequency—in the yrast band of ^{126}I (Band 3 in Fig. 4) [14]. The projection of the total angular momentum along the rotation axis (I_x) can be written as

$$I_x = R + i_x \quad (15)$$

and

$$I_x = \sqrt{I(I+1) - K^2}, \quad (16)$$

where R is the core angular momentum and i_x is the aligned angular momentum of valence particles along the rotation axis. We assumed the Nilsson quantum number $K = 6$ [14], also mentioned in Sec. III D. The Harris parametrization [40,41] was used for the core angular momentum (R) (described in the previous section), which is written as

$$R = \zeta_0\omega + \zeta_1\omega^3. \quad (17)$$

The particle alignment becomes

$$i_x = I_x - \zeta_0\omega - \zeta_1\omega^3, \quad (18)$$

which is plotted with the rotational frequency to observe backbending. The rotational frequencies were determined by dividing the γ energy of $E2$ transitions (Fig. 4) by 2 units of spin difference. Figure 12 presents the alignment plot, marked at the backbending frequency of 0.47 MeV near to the signature inversion point. To describe the observed backbending, we carried out the TRS [39,42] calculation using the computer code ULTIMATE CRANKER [43,44]. Within the Nilsson-Strutinsky prescription—by adding shell effects and pairing to the liquid-drop energy—the cranking model was employed; wherein the nucleus is assumed to be a rigid body and rotating around the principal axes. For a rigid-body rotation, the moment of inertia is highest for the rotation around the shortest axis and hence favored energetically.

Apart from the axial deformation and triaxiality parameters β and γ , the hexadecapole deformation parameter β_4 was also needed in the calculation. We assumed β_4 to be 0. All the other parameters were kept at their default values except Δ_p (pairing gap for proton) and Δ_n (pairing gap for neutron). Their values were varied from 0.8 to 1.1 MeV before deciding finally $\Delta_p = 1.1$ MeV and $\Delta_n = 1.0$ MeV.

At first we attempted to get the single-particle Routhians from the TRS calculation at the deformation values $\beta = 0.15$ and $\gamma = -10^\circ$ corresponding to below inversion. But we

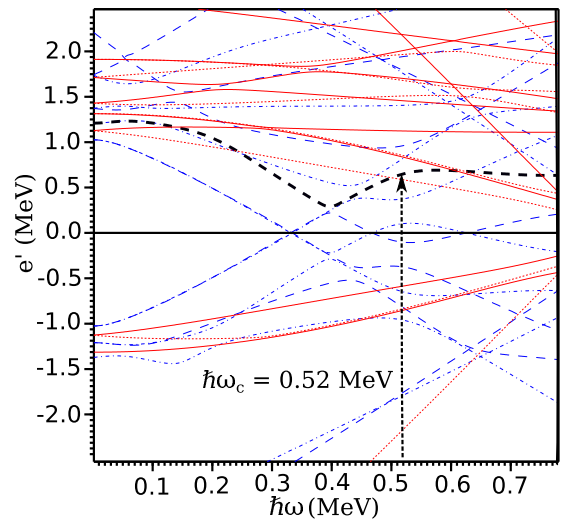


FIG. 13. Neutron Routhian plot at the deformation values $\beta = 0.15$ and $\gamma = 25^\circ$ (above inversion) from the TRS calculation using the computer software ULTIMATE CRANKER [43,44]. The arrow marks the second crossing frequency at $\hbar\omega = 0.52$ MeV. Various curves are marked according to their parity and signature: solid (+, +1/2), dotted (+, -1/2), dash-dotted (-, +1/2), and dashed (-, -1/2).

could not get the crossing frequency within the measured range. Interestingly, we could explain the observation of backbending when we used the deformation values $\beta = 0.15$ and $\gamma = 25^\circ$ corresponding to above inversion, and Fig. 13 presents the neutron Routhian plot. The yrast negative-parity states were built by a quasineutron and a quasiproton occupying the negative-parity and positive-parity Nilsson orbits, respectively. We found the lowest available quasineutron Nilsson state $h_{11/2}[5\ 5\ 11/2\ 9/2]$ with a second backbend at 0.52 MeV (arrow in Fig. 13), which compares well with the experimental value of 0.47 MeV in Fig. 12. The first neutron backbend was blocked because of the odd number of neutrons. Also, the second proton backbend occurred at a much higher frequency theoretically and was unlikely for the observed backbend.

V. CONCLUSION

We have measured the short lifetimes of eight negative-parity yrast states of ^{126}I using the Doppler-shift attenuation method. Two data analysis procedures—gating above (GTA) and gating below (GTB)—have been utilized to obtain the lifetime results independently. The GTA analysis is free from any side-feeding parameter but suffers from somewhat low statistics, whereas the reverse is the case for the GTB analysis. Moreover, using a target without any backing material in our experiment, we were faced with an additional uncertainty due to continuous production and stopping of the recoiling nuclei. Nevertheless, using both GTA and GTB, we obtained the reliable result—a sharp decrease in the reduced transition probabilities $B(E2)$ at the signature inversion. The shape parameters were deduced in the Lund convention, $\beta = 0.15$ and $\gamma = -10^\circ$ below the inversion and $\beta = 0.15$ and $\gamma = +25^\circ$ above it. The results implied only a difference of 15°

in the absolute value of the triaxiality parameter (γ) with a change in sign. Physically, the nuclei changed their shape at the inversion point from near prolate to more like triaxial with a shift in the axis of rotation.

Using the above deformation parameter values, we performed the two quasiparticle-plus triaxial rotor model calculation. The calculation correctly reproduced the phase of signature splitting. However, the extent of splitting was small below the inversion point by the calculation as compared to the experimental observation. The trend in $B(E2)$ values, especially at the signature inversion, was also well reproduced by the calculation. The valence particle configuration for the band was found to be predominantly $\pi d_{5/2} \otimes \nu h_{11/2}$ admixed with $\pi g_{7/2} \otimes \nu h_{11/2}$. To explain the observed backbending, we generated plots of single-particle Routhians for the neutron as well as the proton at the mentioned shape parameter values found above the signature inversion. The second crossing

frequency for the valence proton was way up compared to the observed backbending frequency of 0.47 MeV, whereas it matched reasonably well for the valence neutron, implying neutron alignment.

ACKNOWLEDGMENTS

The authors wish to gratefully acknowledge help from the following colleagues: Virendra Kumar Pasi and Bhushan Bhujang for participating in the experiment, the Pelletron staff for the smooth running of accelerator, Deepa Thapa and A. Mahadkar for target preparation, and Swati Modi for theoretical discussions. The Department of Science and Technology (Grant No. IR/S2/PF-03/2003-III), Government of India, is thankfully acknowledged for the Indian Gamma Array Collaboration.

-
- [1] T. Koike, K. Starosta, C. J. Chiara, D. B. Fossan, and D. R. La Fosse, *Phys. Rev. C* **67**, 044319 (2003).
- [2] V. Kumar, P. Das, S. Lakshmi, P. K. Joshi, H. C. Jain, R. P. Singh, R. Kumar, S. Muralithar, and R. K. Bhowmik, *Phys. Rev. C* **82**, 054302 (2010).
- [3] K. Starosta *et al.*, *Phys. Rev. Lett.* **86**, 971 (2001).
- [4] F. G. Kondev *et al.*, *Phys. Rev. C* **59**, 3076 (1999).
- [5] D. J. Hartley *et al.*, *Phys. Rev. C* **63**, 041301(R) (2001).
- [6] Y. Liu, J. Lu, Y. Ma, S. Zhou, and H. Zheng, *Phys. Rev. C* **54**, 719 (1996).
- [7] R. Bengtsson *et al.*, *Nucl. Phys. A* **415**, 189 (1984).
- [8] I. Hamamoto, *Phys. Lett. B* **235**, 221 (1990).
- [9] A. Ikeda *et al.*, *Nucl. Phys. A* **480**, 85 (1988).
- [10] A. Ikeda and T. Shimano, *Phys. Rev. Lett.* **63**, 139 (1989).
- [11] A. K. Jain *et al.*, *Phys. Lett. B* **277**, 221 (1990).
- [12] A. Goel *et al.*, *Nucl. Phys. A* **620**, 265 (1997).
- [13] R. L. Auble, *Nucl. Data Sheets* **9**, 125 (1973).
- [14] B. Kanagalekar, P. Das, B. Bhujang, S. Muralithar, R. P. Singh, and R. K. Bhowmik, *Phys. Rev. C* **88**, 054306 (2013).
- [15] C. B. Moon *et al.*, *J. Korean Phys. Soc.* **44**, 244 (2004).
- [16] Y. Zheng *et al.*, *Phys. Rev. C* **86**, 014320 (2012).
- [17] T. K. Alexander *et al.*, *Adv. Nucl. Phys.* **10** (1978).
- [18] P. J. Nolan *et al.*, *Annu. Rev. Nucl. Part. Sci.* **38**, 533 (1988).
- [19] P. Petkov *et al.*, *Nucl. Instrum. Methods Phys. Res., Sect. A* **437**, 274 (1999).
- [20] P. Petkov *et al.*, *Nucl. Instrum. Methods Phys. Res., Sect. A* **488**, 555 (2002).
- [21] F. Brandolini and R. V. Ribas, *Nucl. Instrum. Methods Phys. Res., Sect. A* **417**, 150 (1998).
- [22] S. Muralithar *et al.*, *J. Phys.: Conf. Ser.* **312**, 052015 (2011).
- [23] B. P. Ajith Kumar, E. T. Subramaniam, K. M. Jayan, S. Mukherjee, and R. K. Bhowmik, in *Proceedings of the Symposium on Advances in Nuclear and Allied Instruments, India, 1997* (Tata McGraw-Hill, New Delhi, 1997), pp. 51–55.
- [24] <http://www.tifr.res.in/~pell/lamps.html>.
- [25] E. O. Lieder *et al.*, *Eur. Phys. J. A* **35**, 135 (2008).
- [26] J. F. Ziegler *et al.*, *Nucl. Instrum. Methods Phys. Res., Sect. B* **268**, 1818 (2010).
- [27] S. Takeuchi *et al.*, *Nucl. Instrum. Methods Phys. Res., Sect. A* **763**, 596 (2014).
- [28] J. Srebny *et al.*, *Nucl. Phys. A* **683**, 21 (2001).
- [29] J. C. Wells and N. R. Johnson, ORNL Report **6689**, 44 (1991).
- [30] L. C. Northcliffe and R. F. Schilling, *At. Nucl. Data Tables* **7**, 233 (1970).
- [31] J. Lindhard *et al.*, *Mat.-Fys. Medd. K. Vidensk. Selsk.* **33**, 1 (1963).
- [32] J. Lindhard *et al.*, *Mat.-Fys. Medd. K. Vidensk. Selsk.* **33**, 1 (1963).
- [33] J. Lindhard *et al.*, *Mat.-Fys. Medd. K. Vidensk. Selsk.* **36**, 1 (1968).
- [34] C. S. Wu, J. Y. Zeng, Z. Xing, X. Q. Chen, and J. Meng, *Phys. Rev. C* **45**, 261 (1992).
- [35] C. J. Gallagher, Jr., and S. A. Moszkowski, *Phys. Rev.* **111**, 1282 (1958).
- [36] S. E. Larsson, *Phys. Scr.* **8**, 17 (1973).
- [37] S. E. Larsson *et al.*, *Nucl. Phys. A* **307**, 189 (1978).
- [38] I. Ranganarsson (private communication).
- [39] G. Andersson *et al.*, *Nucl. Phys. A* **268**, 205 (1976).
- [40] S. M. Harris, *Phys. Rev. Lett.* **13**, 663 (1964).
- [41] S. M. Harris, *Phys. Rev.* **138**, 3B (1965).
- [42] V. M. Strutinsky, *Nucl. Phys. A* **95**, 420 (1967).
- [43] T. Bengtsson, *Nucl. Phys. A* **496**, 56 (1989).
- [44] T. Bengtsson, *Nucl. Phys. A* **512**, 124 (1990).